Vision, Modeling, and Visualization (2010)

Visualization of Effective Connectivity of the Brain

Sebastian Eichelbaum[1], Alexander Wiebel[2], Mario Hlawitschka[3], Alfred Anwander[2], Thomas Knösche[2] and Gerik Scheuermann[1]

[1]Institut für Informatik, Universität Leipzig, Germany
[2]Max Planck Institute for Human Cognitive and Brain Sciences, Leipzig, Germany
[3]Department of Computer Science, University of California, Davis, CA, USA

Abstract

Diffusion tensor images and higher-order diffusion images are the foundation for neuroscience researchers who are trying to gain insight into the connectome*, the wiring scheme of the brain. Although modern imaging devices allow even more detailed anatomical measurements, these pure anatomical connections are not sufficient for understanding how the brain processes external stimuli. Anatomical connections constraint the causal influences between several areas of the brain, as they mediate causal influence between them. Therefore, neuroscientists developed models to represent the causal coherence between several pre-defined areas of the brain, which has been measured using fMRI, MEG, or EEG. The dynamic causal modeling (DCM) technique is one of these models and has been improved to use anatomical connection as informed priors to build the effective connectivity model. In this paper, we present a visualization method allowing neuroscientists to perceive both, the effective connectivity and the underlying anatomical connectivity in an intuitive way at the same time. The metaphor of moving information packages is used to show the relative intensity of information transfer inside the brain using a GPU based animation technique. We provide an interactive way to selectively view one or multiple effective connections while conceiving their anatomical connectivity. Additional anatomical context is supplied to give further orientation cues.*

Categories and Subject Descriptors (according to ACM CCS): Computer Graphics [I.3.3]: Display algorithms—Computer Graphics [I.3.7]: Animation—

1. Introduction

Diffusion-weighted magnetic resonance imaging (DW-MRI) has become a window to the anatomical structures of the human brain and allows *in-vivo* reconstruction of fiber tracts that form neural networks. Although the size of single nerve fibers is far below the resolution capabilities of today's imaging devices, neuroscientists use tracked fiber clusters intensively to understand the human brain's structure, in particular its *connectome*, i.e., the wiring scheme of the brain. On the other hand-side, Electroencephalography (EEG), magnetoencephalography (MEG) and functional MRI (fMRI) allow scientists to measure functional coherences between the activation in different brain areas in response to external stimuli.

A major goal in biology, medicine, and, in particular, neuroscience is the understanding of structure-function relationships. To combine both, the anatomical knowledge and the experimental results and to model the influences of structural connections in an experimental context, many approaches have been developed. One of these models is Dynamic Causal Modeling (DCM) [FHP03] which can be seen as a generalization of structural equation modelling [MGL94]. The basic idea is to find a reasonable model that represents interacting cortical regions. DCM aims at making estimations about the causal architecture of coupled brain regions and, even more interesting, how this coupling is influenced by experimentally induced stimuli. In 2009, Stephan et. al. [STK*09] introduced an approach to include tractography-based anatomical knowledge into DCM and has provided the first formal evidence that anatomical knowledge can improve DCM.

As a result, effective connectivity can be calculated between the cortical regions used in the setup, denoting the actual information transfer between these regions. It is a measure for causal relation between two regions. For each pair of regions A and B connected anatomically, two effec-

© The Eurographics Association 2010.

tive connectivity values can be computed, one in each direction along the same anatomical path, i.e. a directed effective connectivity describing the information transfer from A to B and one from B to A. These models are usually represented visually as a graph, where each node represents a certain area of the brain and is connected to other nodes with directed, weighted edges, denoting the effective connectivity. Two-dimensional graph layouts do not allow the inclusion of anatomically guided geometric relationships and are, therefore, not able to show the structure–function relationship properly. Additionally, the visualization of two values in opposing directions on the same anatomical connection is a serious problem for common visualization methods.

In this paper, we present a method to circumvent the above problems. We combine anatomical and effective connectivity to embed the DCM model into its underlying anatomical context. The anatomical pathways, transporting the information between each pair of connected regions, get extracted and used to project the effective connectivity using an animation technique for relative visualization of up to two effective connectivity values at the same time.

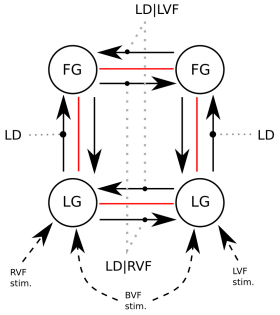

Figure 1: *Example effective connectivity graph. Shown are the involved regions, fusiform gyrus (FG) left and right as well as lingual gyrus (LG) left and right. The regions are connected anatomically (red) and, as modelled in the DCM model, by effective connections. The connection modulation (gray dotted lines) has been modeled by task and stimulus properties. Several stimuli have been applied as individual events to the lingual gyrus in the left visual field (LVF), right visual field (RVF) and both visual fields (BVF). For more details, see [SMP*07].*

2. Related Work

Visualization of medical data is a wide-spread field and many approaches have been developed to visualize almost all imaging and measurement modalities separately or in conjunction with each other.

In the context of our work, methods regarding several kinds of connectivity are of special interest. Fiber tractography has been introduced to provide a global view on locally acquired data [BPP*00]. To interactively explore the white matter pathways, it has proven advantageous to pre-calculate a large number of fiber tracts in advance and selectively filter them by using regularly shaped regions of interest [ASM*04, BBP*05]. Another approach is to create large-scale structural brain networks describing anatomical connection between several cortical regions of the brain [HCG*08]. These networks can be visualized by graphs and even by embedding them into the three-dimensional context of the brain, where they can be explored interactively [GCTH10].

Functional connectivity is another challenge. The vast amount of data requires statistical methods to find significant relations, which can be understood best by providing an underlying anatomical context and interactive tools to selectively view the information provided [MWZ*00, WMZ*01].

For visualization of volumetric data, the marching cubes algorithm [LC87] and direct volume rendering (e.g., [EHK*06]) are common methods of choice. Surface-based approaches, which are able to ray-trace an isosurface in real-time [KWH09], are of special interest for our approach because we use surfaces to show effective connectivity on it and for providing anatomical context.

3. Motivation

To understand the need for a new kind of visualization, one needs to understand the difference between effective connectivity and, for example, anatomical connectivity.

As anatomical connections can be seen as an undirected graph, fiber tracts or three-dimensionally embedded graphs are the visualization methods of choice. In contrast, the graph representing effective connectivity is a weighted graph (cf. Figure 1), where effective connectivity is the weight on each edge. Along one anatomical connection, two contrarily directed effective connectivity values may need to be visualized. This requirement rules out several standard techniques to quantitatively visualise directed information as they are not able to properly show two quantities in contrary directions. Besides nearly trivial methods like color-coding of fiber tracts or visualization by arrows, this also accounts for particle animation [KKKW05] , line integral convolution (LIC) [CL93] or GPU based advection [LJH03, TvW03] methods. In any case, Holten and van Wijk [HvW09] analyzed several possibilities to show directed information and found that standard arrow representation should be avoided and color-/intensity-/transparency-gradient-based visualization is not free of ambiguities. It also states the potential of animation for representation of direction.

Our neuroscientist collaboration partners required an intuitive and, at the same time, appealing visualisation with a more illustrative and metaphoric character than a precise visualization of quantity values. The metaphor of moving "information packages" on their underlying anatomical connec-

© The Eurographics Association 2010.

tion meets this requirements best and embodies the meaning of effective connectivity perfectly.

Although we present a visualization for effective connectivity, one should always keep in mind that visualization represents only a model of reality. The exact modalities of physiological information transfer inside the brain are not known by now.

4. Method

Now, as the terms of effective and anatomical connectivity has been described, including some specialties and their calculation, we will continue with how we extract the fiber tract cluster, building the foundation for our anatomically based visualization. Following next is the volumization of the previously selected fiber tract cluster and the post-processing of the volume data, which is then used for animating effective connectivity on an isosurface in the volumized fiber tract data.

In the following sections, the effective connectivity graph is handled as a weighted directed graph: (V,A,e). Each node $r \in V$ is anatomically represented by a region of the brain and each arc $c \in A$ correlates with a cluster of fiber tracts, corresponding to the anatomical connection. The weighting function $e(i,j)$ provides the directed effective connectivity value for each connected pair of regions r_i and r_j. Another convention we will use in the following sections is to treat each fiber tract as an ordered sequence of points: $f = \{x | x \in \mathbb{R}^3\}$ in the set of all fiber tracts $f \in F$. In a real-world dataset, this ordering is defined by the set of line segments $f^{segments} = \{(a,b) | a,b \in f\}$. This set also defines two designated elements:

$$f_{x_0} \in f \text{ with } \neg\exists w \in f : (w, f_{x_0}) \in f^{segments} \text{ and} \quad (1)$$

$$f_{x_{|f|-1}} \in f \text{ with } \neg\exists y \in f : (f_{x_{|f|-1}}, y) \in f^{segments}, \quad (2)$$

denoting the first and the last vertex of the fiber tract if the order in f is assumed to be the order of appearance of each vertex along the tract ($f^{segments}$).

4.1. Fiber Tract Selection

As the graph in Figure 1 implies, the anatomical connection is always defined between two distinct areas of the brain. These regions need to be known beforehand and can be extracted in several ways. In our example, the *fusiform gyrus* and *lingual gyrus* have been segmented manually. An alternative to manually segmenting the required regions is the use of atlas-based methods (e.g., [RBM*05]).

With the help of the segmented regions, the selection of all fiber tracts, belonging to the anatomical connections in A, can be done by checking whether a fiber $f \in F$ connects the regions r_i and r_j with $r_i, r_j \in V$ and, therefore, by classifying them to belong to a cluster $C_{(r_i,r_j)}$. To actually perform this selection, Blaas et. al. [BBP*05] presented a fast selection method for regular masks, boxes in their case. As our classification needs to be done with irregular masks and needs to be computed only once, such optimization strategies are not worth the additional computational effort. Each fiber tract can be classified very fast by simply testing each fiber tract's vertices $x \in f \in F$ against both regions r_i and r_j while loading the pre-integrated fiber tract data set. Additionally, vertices get discarded if they are not inside one of the regions or between them to cut away parts not needed to represent the anatomical connection between both areas. As this fiber selection is straight forward, besides some issues regarding the sampling theorem, we omit the details here.

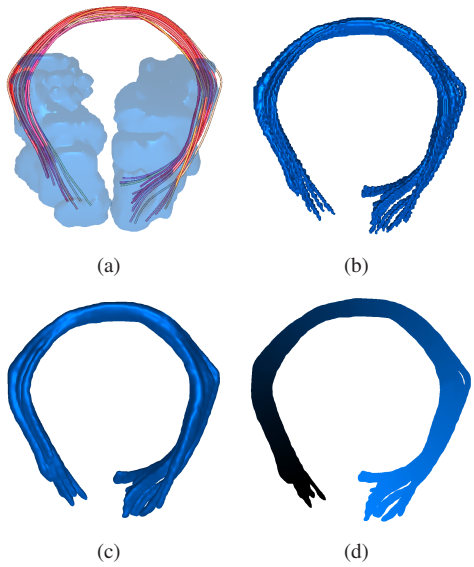

Figure 2: *The selected part of the* forceps occipitalis *(a) selected by LG left and LG right volumized (b) and filtered using one iteration of the Gaussian filter (c). Applying the Gaussian filter once yields a smooth surface, maintaining the anatomical structure. The parameterization (d) is used to characterize the main direction of the fiber tract cluster at each point in the volume.*

Figure 2(a) shows a part of the forceps occipitalis selected by the left and right lingual gyrus, supplemented with the corresponding masks.

4.2. Fiber Tract Volumetric Representation

Depending on the location of the selection regions $r \in V$ in the brain, the amount and density of the fibers may vary. This again becomes problematic for surface based animation. The animation might not even be perceptible if the fiber tract cluster is too thin or too sparse. To avoid this problem, we create a volume out of the cluster. The volume can then be post-processed to close holes or for thickening the

© The Eurographics Association 2010.

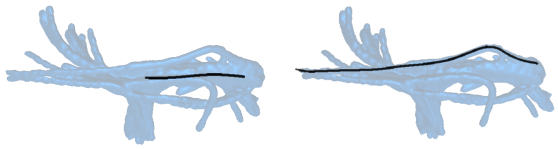

(a) Centerline (b) Longest fiber-tract

Figure 3: *The fiber tracts between the right fusiform gyrus and the right lingual gyrus. Left: the centerline is too short to properly parameterize the volume along the main direction of the bundle. Right: the longest line solves the problem but it is not necessarily in the center of the bundle.*

cluster's volumetric representation. An alternative is the approach by Enders et. al. [ESM*05], which calculates a wrapping surface around the fiber tracts. However, it may create surfaces not wrapping the whole cluster, especially if it contains strongly diverging fiber tracts.

Voxelization of three-dimensional lines and line segments is covered in many publications. We are basically using a three-dimensional variant of the Bresenham algorithm [Bre65] for line rasterization with anti-aliasing similar to the idea in Wu's line algorithm [Wu91]. As both algorithms are sufficiently well known, we do not go into details here.

Volumizing all fiber tracts $f \in C_{(r_i,r_j)}$ for all $(r_i,r_j) \in A$ yields in several three dimensional discrete fields describing the anatomical paths of information transfer for each connected regions r_i and r_j:

$$v_{(r_i,r_j)}(x,y,z) \in [0,1]. \tag{3}$$

Figure 2(b) shows the resulting volume as an isosurface. The surface is very rough and, therefore, does not look natural. Applying a single discrete Gaussian filter iteration to the volumized fiber tracts $v_{(r_i,r_j)}(x,y,z)$ smoothes the surface while keeping the anatomical structure of the fiber-tract cluster. The isovalue used in both examples is 0.3, as both datasets are in the interval of $[0,1]$.

Until now, there is no information about the direction, nor the tangential information of the underlying fiber tract cluster available during rendering. A second volume containing a parameterization of the fiber tract cluster itself is needed. We first tried using the centerline described in [ESM*05], which is there used to calculate a wrapping surface around a fiber tract cluster. Caused by quickly diverging tracts, or short tracts that are distributed along the fiber tract cluster, the centerline degenerates to a short line which is not going through the whole tract cluster. The fiber tracts between the right fusiform gyrus and the right lingual gyrus are an example for this, as Figure 3(a) shows.

The longest fiber tract in the cluster, called f^{param}, is selected for parameterization, which works properly, even though the longest line might not be in the center of the cluster, nor represents it the main direction of the cluster. In all the datasets we have used so far, this was no problem and is, therefore, negligible.

To finally parameterize the volumized fiber tract cluster, an additional $parameterize_{f^{param}}(x,y,z)$ function is used which calculates the parameter for a given point in relation to the parameterization fiber tract f^{param}. The parameterization field p is then similar to $v_{(r_i,r_j)}(x,y,z)$ defined voxel-wise:

$$p_{(r_i,r_j)}(x,y,z) = parameterize_{f^{param}}(v_{(r_i,r_j)}(x,y,z)). \tag{4}$$

The function *parameterize* itself is defined the following:

$$parameterize_{f^{param}}(x,y,z) = \underbrace{|f^{param}_{x_0},\ldots,x_{nearest}|}_{\text{length of } f^{param} \text{ if cut at } x_{nearest}}. \tag{5}$$

The fiber tract vertex $x_{nearest} \in f^{param}$ is the nearest vertex of the parameterization fiber tract to the voxel (x,y,z). So, the length of the parameterization fiber tract up to the voxel's nearest vertex parameterizes the cluster. The parameterization field needs to be scaled down from the interval $[0,|f^{param}|]$ to the interval $[0,1]$ to allow it to be uploaded to the graphics hardware as an texture as $p^{scaled}_{(r_i,r_j)}$. Figure 2(d) shows the parameterization of the masked part of the *forceps occipitalis* using color coding.

As the volumized fiber tract field $v_{(r_i,r_j)}(x,y,z)$ was smoothed earlier, the parameterization field $p_{(r_i,r_j)}(x,y,z)$ needs be calculated only for those voxels with a value not zero and can be done during the Gaussian filter iteration. This ensures a continuous parameterization for all voxels involved in the anatomical path.

4.3. Effective Connectivity Animation

After the fiber tracts have been selected and volumized, a smooth surface can be rendered. Typically, the marching cubes algorithm [LC87] is used for triangulation of volume data. Although our animation approach works on triangulated surfaces too, we are using a GPU-based ray tracing [EHK*06] for isosurface extraction and rendering. With this approach, we circumvent any possible triangulation-related problems and achieve a topological correct surface, which renders even the thinnest fiber tract branches correctly. As this kind of volume rendering is well known, we omit the details here. Figure 2(b) shows the GPU ray traced isosurface with gradient based per pixel lighting.

As the parameterization field was uploaded to the GPU too, we apply effective connectivity animation on the GPU for every fragment on the surface by classifying each surface pixel to belong to either the highlighted pixels, highlight-border pixels or to the non-highlighted part of the surface. Those highlighted beams, representing the "information-packages", move from r_i to r_j and vice versa with different

© The Eurographics Association 2010.

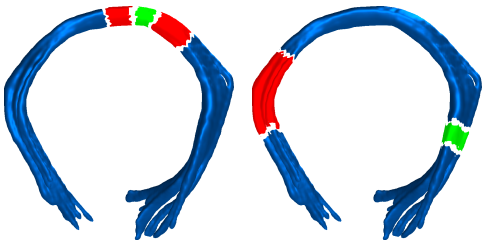

(a) With overlapping (b) No overlapping

Figure 4: *The final rendering of the fiber tract cluster from left to right lingual gyrus with both effective connectivity beams. For a video showing the animation, take a look at the supplemental material accompanying this paper. Left: This image was made at a time-step where the beams of LG left→LG right and LG left←LG right do overlap to show how we combine both beams. Right: without overlapping at another time-step.*

size to represent the effective connectivity. Please take a look in the supplemented material accompanying this paper to see the animation.

To ease the following description up, we will describe only one moving package in the direction r_i to r_j along the corresponding anatomical connection in $v_{(r_i,r_j)}(x,y,z)$. In the next paragraphs, we call those "packages" only "beams" as they look similar to moving beams on the surface. Due to the graphics hardware architecture, only one fragment can be processed at a time. Neighboring pixels are not accessible for write or for read. This is why we need to calculate the current midpoint of the "information-package" for each fragment:

$$m = ((t+o)*v) \; mod \; (k+\frac{k}{3}) - \frac{k}{6} \tag{6}$$

The Equation 6 is very simple and uses two parameters. The current time t with an offset o in milliseconds and the velocity v. It is the well known physical relationship between distance, time and velocity. The offset parameter is used to avoid that the beam $r_i \rightarrow r_j$ starts at the same moment as the beam $r_i \leftarrow r_j$ starts. This creates a better impression as it does not look as artificial as if they would have been started at the same time, meeting both exactly in the middle of the cluster. The modulo operation ensures that there is a periodic beam-movement from r_i to r_j along the current voxel's gradient in parameterization space in k units along the fiber tract cluster. In our implementation we are using $k = 100$, which creates a smooth movement. To ensure that the beam does not abruptly end when the middle of the beam reaches the end of the cluster and to ensure that the beam does not pop up on the other side with the beam's middle at the beginning of the cluster, the interval is stretched. The value of m then also covers the invisible part of the parameter space, large enough to contain half of a beam's maximum size, in this case $\frac{k}{6}$ on each end of the parameter space. For more details on the size of the beams, see section 4.3.1. The value of m then represents the current position of the beam as a line perpendicular to the main direction (the current gradient) on the surface. This line moves, depending on time and speed, along the surface and is then used for classifying the current fragments parameter in $p_{(r_i,r_j)}(x,y,z)$ (recall that the parameterization field in Equation 7 is scaled to the interval $[0,1]$ to be uploaded as $p^{scaled}_{(r_i,r_j)}(x,y,z)$ in a texture), whether it belongs to the current beam, or "information package":

$$b_{(r_i,r_j)}(x,y,z) = |m - k * s_{(r_i,r_j)} p^{scaled}_{(r_i,r_j)}(x,y,z)| - \frac{l_{(r_i,r_j)}}{2}. \tag{7}$$

Equation 7 describes an environment of size $l_{(r_i,r_j)}$ (the length of the beam from r_i to r_j) around the current beam-center m and describes a predicate for each fragment at the current coordinate whether it is inside the beam ($b < -\varepsilon$), on the border of the beam ($b \in [-\varepsilon, 0]$) or outside of it ($b > \varepsilon$), where ε denotes the border width. Ignoring the additional parameter s, this simply tests whether the actual fragment along the main direction of the fiber tract cluster is near the current position m. The parameter s is used to ensure equal speeds and the correct size-relation between the beams for all beams on all fiber tract clusters and is the relation between the fiber used for parameterization of the cluster (r_i, r_j) and one of the parameterization fibers of all the clusters in A:

$$s_{(r_i,r_j)} = \frac{|f^{param}_{(r_i,r_j)}|}{|f^{param}_{ref}|}, (r_i,r_j) \in A, \text{ref} \in A. \tag{8}$$

The final pixel color can finally be determined using an arbitrary color map. In our implementation, we use the following mapping:

$$c_{fragment} = \begin{cases} c_{(r_i,r_j)} \text{ if } & b_{(r_i,r_j)} < -\varepsilon \\ c_{(r_j,r_i)} \text{ if } & b_{(r_j,r_i)} < -\varepsilon \\ c_{(r_i,r_j)} \text{ if } & b_{(r_i,r_j)} < -\varepsilon \wedge \\ & b_{(r_j,r_i)} < -\varepsilon \wedge \\ & l_{(r_i,r_j)} \leq l_{(r_j,r_i)} \\ c_{(r_j,r_i)} \text{ if } & b_{(r_i,r_j)} < -\varepsilon \wedge \\ & b_{(r_j,r_i)} < -\varepsilon \wedge \\ & l_{(r_i,r_j)} > l_{(r_j,r_i)} \\ white \text{ if } & b_{(r_j,r_i)} \in [-\varepsilon, 0] \\ c_{surface} & \text{else} \end{cases} \tag{9}$$

The surface itself has a user defined color $c_{surface}$, which is set if the fragment does not belong to either one of the beams and is shaded by a previously calculated per-pixel Phong shading. Equation 9 also covers the case where the beams overlap. If this is the case, the color of the smaller beam is used. Blending both colors would irritate the user too much. The white border around each beam ensures that the beam is visible even if the contrast between the beam's color $c_{(r_i,r_j)}$ or $c_{(r_j,r_i)}$ and the surface color is very low. Figure 4 shows two time-steps of the animation, one with overlapping beams.

© The Eurographics Association 2010.

4.3.1. Determining the length of the beams

The effective connectivity represented by the specific beam is used to define its length. To have the length and, especially, their relation between each other consistent, we map the interval $[0,1]$, representing the smallest and largest beam to the interval of the involved effective connectivities (the connectivity graph's weighting function e):

$$[min\{e(i,j)|(r_i,r_j) \in A\}, max\{e(i,j)|(r_i,r_j) \in A\}] \quad (10)$$

The mapping function has to map between $[0,1]$ and the interval of the smallest to the largest connectivity value. This mapping can be adapted to the possible cases. In our examples, the effective connectivities do not spread wide in $\mathbb{R}$ and, therefore we use a linear mapping. If the effective connectivities vary very strongly, a logarithmic scale can help to avoid many very small beams of not distinguishable size and very few large beams. It is worth mentioning, that the beam length interval $[0,1]$ itself needs to be mapped to the actual beam sizes. This mapping is strongly dependent to the parameter k of the above equations 6 and 7. A good choice is to set the beam sizes to $[\frac{k}{100}, \frac{k}{3}]$ which creates beams not too small and avoids extremely large beams covering the whole surface.

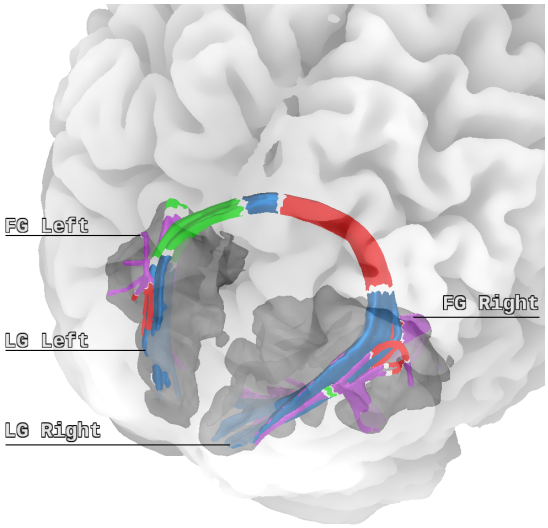

Figure 5: *The final rendering of the T1 context and the effective connectivity graph from Figure 1. The involved regions are labeled and the fiber tract cluster are colored differently. To properly understand the image, the animation is required. The animation provides the direction and, therefore, the source and target of an "information package".*

4.4. Labeling

Due to the scaling and the movement of the beams on the surface, it is difficult to read the actual effective connectivity value. Only relationships can be seen. Therefore, our approach is supplemented with some labeling features, allowing the user the see the real effective connectivity value and the names of the involved regions. To avoid, that the labels overlap the actual surface and animation, we have implemented a boundary based labeling, similar to the one in [BKSW04]. We arrange labels with the name of the regions on the boundary of the bounding box enclosing the whole scene.

Figure 5 and 6 shows the example fiber tract cluster with the corresponding labels. The video accompanying the paper shows the dynamics of label placement.

5. Results

In this section, we demonstrate our method for two different types of datasets: a real data set (cf. Figure 5 and 6) obtained by DCM with tractography-based priors and an artificial data set (cf. Figure 7). We use artificial data to show the method in more complex environments. The data taken from [STK*09] and [SMP*07] examined only the connection of a region in one hemisphere and the connectivity to their relatively close counterpart in the other hemisphere (see Figure 1).

5.1. Data

5.1.1. DCM Data

The diffusion data used for fiber tracking is a DTI measurement with 60 directions acquired with a three Tesla scanner at the Max Planck Institute for Human Cognitive and Brain Sciences. The DTI image is given as second-order tensor data, $93 \times 116 \times 93$ voxels with a resolution of 1.72 mm. The tracts we use were computed using the method of Weinstein et al. [WKL99]. The complete set of tracts consists of 74,313 tracts, represented by 5,472,306 vertices. The FG and LG, left and right, were segmented in an MRI T1 image measured using the same three Tesla scanner as used for the DTI data. The image, warped into standard space, has a resolution of 1mm for $160 \times 200 \times 160$ voxels.

The subsequent selection of the fiber tracts connecting the regions yielded only three of the links shown in Figure 1. The link between FG left and FG right is missing. This results from the low probability of this connection (see Figure 1) together with the parameter setting of our deterministic tracking. Neuroscientists, who perform studies about effective connectivity, however, are able to fit their probabilistic tracking used to estimate the probabilities to a deterministic fiber tract dataset. Thus, the missing link is not a result of our method, which is still useful without the missing link.

© The Eurographics Association 2010.

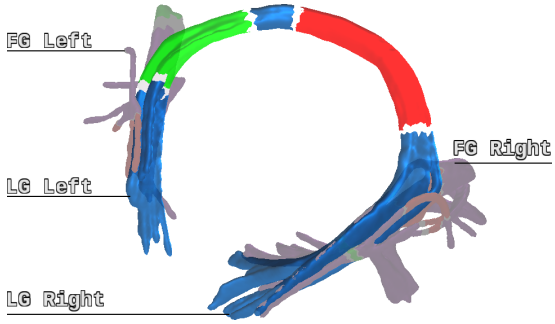

(a) focusing LG left - LG right

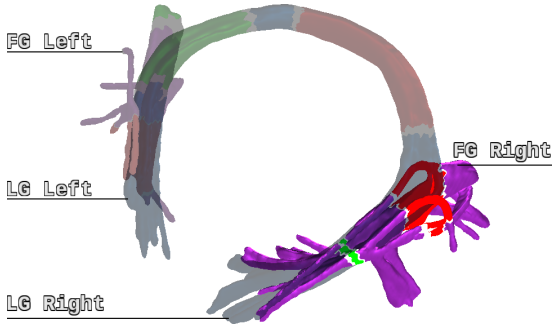

(b) focusing LG left - FG right

Figure 6: *The user can selectively explore the effective connectivity graph, by highlighting the needed parts of the graph. Transparency also helps to explore occluded parts of other fiber tracts or to unveil interpenetrated tracts.*

Fiber tract cluster	FPS
Whole connectivity graph (Figure 5)	12
Whole connectivity graph, no context (Figure 6)	22
Artificial data with context (Figure 7(a))	18
Artificial data with context (Figure 7(b))	14

Table 1: *Performance of the rendering in frames per second (FPS).*

5.1.2. Artificial Data

For the artificial example we took the same tract and T1 anatomy data as above but selected arbitrary regions. The connectivity for the tract connection between these regions was chosen randomly. This approach allowed us to produce complex, yet expressive connections that help to illustrate our method. Figure 7 shows two examples of artificial data. Even though, these examples are not necessarily realistic, they prove that our method is not only applicable to some special physical connections and effective connectivity graphs.

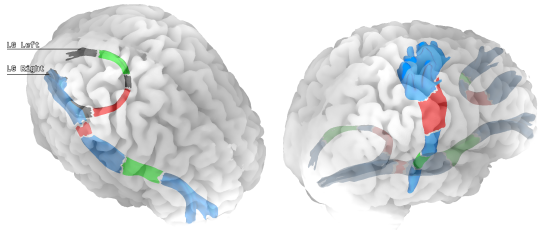

(a) (b)

Figure 7: *Artificial test data for illustration: Figure (a) shows the LG left – LG right fiber tract and the tract resulting from using the LG right – FG right regions without cropping the fibers. Figure (b) shows the tracts from (a) and a part of the corticospinal tract and the forceps minor in front of the brain.*

5.2. Performance

The computational effort of the method can be divided into two separate parts: preprocessing (fiber selection and volumization) and rendering. The preprocessing step runs in the order of seconds for all the data sets presented in this paper, and will not be much larger for any data of reasonable size. Thus, the effort is in the same range as loading the data and is consequently negligible.

The rendering step is entirely performed on the graphics board. This leads to very efficient computation, yielding interactive frame rates. Table 1 lists some frame rate measurements and the corresponding figure. For measuring these frame rates, we have used a computer with two AMD Quad-Core Opteron processors, 32 GB of RAM and an NVidia GeForce 8800 GTX graphics board. As shown in Table 1, we provide a visualization with high frame rates, so the neuroscientists can interactively explore their data.

5.3. Limitations

Although our method is parameter-free, it strongly relies on segmented data for each of the regions involved into the effective connectivity graph. These segmented regions significantly influence the results of the fiber tract selection process. These selection masks can either be segmented manually or by using an atlas.

6. Conclusion and Further Work

We presented an interactive, animated visualization for illustrating effective connectivity in the human brain. It provides an intuitive and understandable visualization of the involved anatomical structures and the corresponding effective connectivities, by using the metaphor of “information packages”. We provided a parameter-free animation based technique to visualize the directed quantity of effective connectivity in a relative fashion. This helps neuroscientists to

© The Eurographics Association 2010.

see and understand the information transfer between the involved regions in the context of their underlying anatomical context. In complex DCM graphs and networks, the animation can get confusing as many anatomical paths show information-transfer and, therefore, create visual clutter. We avoid visual clutter by allowing the user to selectively view parts of the graph and fading out animation on others thus retaining the other anatomical structures. The incorporation of focus and context principles and interactive selection of parts of the data makes it even more useful for daily use and exploration of data.

An interesting avenue of future research can be the direct incorporation of probabilistic tractography data as used for the studies yielding the effective connectivity values. This can serve as basis for a connection representation instead of the volumized deterministic tracking lines. This would also solve the problem of anatomical connections, not found by the current preprocessing step. We will furthermore evaluate different kinds of animation with our neuroscientist users to possibly find other, even better representations of effective connectivity in its anatomical context.

References

[ASM*04] AKERS D., SHERBONDY A., MACKENZIE R., DOUGHERTY R., WANDELL B.: Exploration of the brain's white matter pathways with dynamic queries. In *IEEE VIS '04* (2004), pp. 377–384. 2

[BBP*05] BLAAS J., BOTHA C. P., PETERS B., VOS F. M., POST F. H.: Fast and reproducible fiber bundle selection in dti visualization. *IEEE VIS '05 0* (2005), 59–64. 2, 3

[BKSW04] BEKOS M. A., KAUFMANN M., SYMVONIS A., WOLFF E.: Boundary labeling: Models and efficient algorithms for rectangular maps. In *Symposium on Graph Drawing (GD'04), LNCS 3383* (2004), pp. 49–59. 6

[BPP*00] BASSER P. J., PAJEVIC S., PIERPAOLI C., DUDA J., ALDROUBI A.: In vivo fiber tractography using dt-mri data. *Magnetic resonance in medicine 44*, 4 (October 2000), 625–632. 2

[Bre65] BRESENHAM J. E.: Algorithm for computer control of a digital plotter. *IBM System Journal 4*, 1 (1965), 25–30. 4

[CL93] CABRAL B., LEEDOM L. C.: Imaging vector fields using line integral convolution. In *SIGGRAPH '93* (1993), pp. 263–270. 2

[EHK*06] ENGEL K., HADWIGER M., KNISS J., REZK-SALAMA C., WEISKOPF D.: *Real-time Volume Graphics*. A K Peters, 2006. 2, 4

[ESM*05] ENDERS F., SAUBER N., MERHOF D., HASTREITER P., NIMSKY C., STAMMINGER M.: Visualization of white matter tracts with wrapped streamlines. In *IEEE VIS '05* (2005), pp. 51–58. 4

[FHP03] FRISTON K., HARRISON L., PENNY W.: Dynamic causal modelling. *NeuroImage 19*, 4 (2003), 1273 – 1302. 1

[GCTH10] GERHARD S., CAMMOUN L., THIRAN J.-P., HAGMANN P.: ConnectomeViewer.org, 2010. Ecole Polytechnique Fédérale de Lausanne and University Hospital Center and University of Lausanne. 2

[HCG*08] HAGMANN P., CAMMOUN L., GIGANDET X., MEULI R., HONEY C. J., WEDEEN V. J., SPORNS O.: Mapping the structural core of human cerebral cortex. *PLoS Biol 6*, 7 (07 2008), e159. 2

[HvW09] HOLTEN D., VAN WIJK J. J.: A user study on visualizing directed edges in graphs. In *CHI '09* (2009), pp. 2299–2308. 2

[KKKW05] KRÜGER J., KIPFER P., KONDRATIEVA P., WESTERMANN R.: A particle system for interactive visualization of 3D flows. *IEEE TVCG 11*, 6 (11 2005), 744–756. 2

[KWH09] KNOLL A. M., WALD I., HANSEN C. D.: Coherent multiresolution isosurface ray tracing. *Vis. Comput. 25*, 3 (2009), 209–225. 2

[LC87] LORENSEN W. E., CLINE H. E.: Marching cubes: A high resolution 3d surface construction algorithm. In *SIGGRAPH '87* (1987), pp. 163–169. 2, 4

[LJH03] LARAMEE R. S., JOBARD B., HAUSER H.: Image space based visualization of unsteady flow on surfaces. In *IEEE VIS '03* (2003), p. 18. 2

[MGL94] MCINTOSH A. R., GONZALEZ-LIMA F.: Structural equation modeling and its application to network analysis in functional brain imaging. *Human Brain Mapping 2*, 1-2 (1994), 2–22. 1

[MWZ*00] MUELLER K., WELSH T., ZHU W., MEADE J., VOLKOW N.: Brainminer: A visualization tool for roi-based discovery of functional relationships in the human brain. In *NPIVM '00* (2000), pp. 481–485. 2

[RBM*05] ROHLFING T., BRANDT R., MENZEL R., RUSSAKOFF D. B., MAURER JR. C. R.: *Handbook of Biomedical Image Analysis: Registration Models*. Springer–Verlag Berlin Heidelberg, 2005, ch. Quo Vadis, Atlas-Based Segmentation?, pp. 435–486. 3

[SMP*07] STEPHAN K. E., MARSHALL J. C., PENNY W. D., FRISTON K. J., FINK G. R.: Interhemispheric Integration of Visual Processing during Task-Driven Lateralization. *J. Neurosci. 27*, 13 (2007), 3512–3522. 2, 6

[STK*09] STEPHAN K. E., TITTGEMEYER M., KNÖSCHE T. R., MORAN R. J., FRISTON K. J.: Tractography-based priors for dynamic causal models. *NeuroImage 47*, 4 (2009), 1628 – 1638. 1, 6

[TvW03] TELEA A., VAN WIJK J. J.: 3D IBFV: Hardware-accelerated 3d flow visualization. In *IEEE VIS '03* (2003), p. 31. 2

[WKL99] WEINSTEIN D., KINDLMANN G., LUNDBERG E.: Tensorlines: advection-diffusion based propagation through diffusion tensor fields. In *VIS '99* (1999), pp. 249–253. 6

[WMZ*01] WELSH T., MUELLER K., ZHU W., VOLKOW N., MEADE J.: Graphical strategies to convey functional relationships in the human brain: a case study. In *VIS '01* (Washington, DC, USA, 2001), pp. 481–484. 2

[Wu91] WU X.: An efficient antialiasing technique. *SIGGRAPH '91 25*, 4 (1991), 143–152. 4

© The Eurographics Association 2010.